

**Velocity scaling of a shock wave reflected off a circular cylinder**E. Glazer,<sup>1</sup> O. Sadot,<sup>1,\*</sup> A. Hadjadj,<sup>2</sup> and A. Chaudhuri<sup>2</sup><sup>1</sup>*Pearlstone Center for Aeronautical Engineering Studies, Department of Mechanical Engineering, Ben-Gurion University of the Negev, Beer Sheva, Israel*<sup>2</sup>*National Institute of Applied Sciences, INSA & CORIA UMR 6614 CNRS, Rouen, France*

(Received 14 February 2011; revised manuscript received 7 April 2011; published 22 June 2011)

Two different approaches are undertaken to investigate the interaction of planar shock waves with circular cylinders. Experiments are conducted in a shock-tube apparatus equipped with a schlieren-based optical system to monitor the interaction, and numerical simulations are carried out using an in-house computer code to simulate similar problems. The incident shock-wave Mach number is varied in the range 1.1–1.4. Excellent agreement is found between the simulations and the experiments in terms of shock patterns, even though the model is based on an inviscid approach. Quantitative comparisons between the experimental results for different initial conditions (shock-wave strength, cylinder diameter, and working gas) are made to find the physical parameters affecting the path of the reflected shock. An approximate universal relation is derived, which predicts the reflected-shock trajectory along the axis of symmetry as a function of the incident-shock Mach, the diameter of the cylinder, and the gas properties. This relation is valid in the vicinity of the cylinder in the range of  $0.1$ – $5 D$ , where  $D$  is the cylinder diameter. It is found that the reflected shock from the cylinder evolves as in the case of a reflected-shock wave from a planar wall multiplied by a reduction factor, which depends on the incident-shock Mach number and the ratio of specific heats.

DOI: [10.1103/PhysRevE.83.066317](https://doi.org/10.1103/PhysRevE.83.066317)

PACS number(s): 47.40.Nm, 07.35.+k, 47.11.–j

**I. INTRODUCTION**

The interaction of shock waves with rigid obstacles has attracted the interest of many researchers during the past few years, because this type of interaction yields a truly complex and unsteady flow. In terms of shock attenuation, the interaction reduces the shock-wave strength and creates three-dimensional and rotational flows behind the obstacle. Consequently, the understanding of this unsteady phenomenon will contribute to the knowledge of more complex processes, such as explosion and blast waves.

In this problem, a planar shock impinges on a finite-length circular cylinder, producing curved reflected and diffracted waves. As time evolves, the interaction generates complicated flow patterns including multiple reflected and scattered shocks, Mach stems, slip lines, vortices, and acoustic waves. This problem has been the subject of a number of analytical, experimental, and numerical investigations (see, for example, Refs. [1–7]). Most attention has been paid to vorticity production resulting from the diffraction process and the interaction between shocks and vortices, which develop downstream of the obstacles.

Regarding the dynamics of the shock-wave reflection, researchers have focused their studies on the type of transition, especially from Mach reflection (MR) to regular reflection (RR). This transition depends on a variety of physical parameters, such as the shape of the obstacle, the shock-wave strength, and the type of gas in which the interaction occurs.

In a pioneering work by Whitham [8], an introduction to the formulation of an approximate theory for the dynamics of two- and three-dimensional shock waves was presented.

Whitham applied this theory to the description of shock diffraction by wedges and corners. The theory is based on the critical angle (angle of transition  $RR \rightarrow MR$ ) and the incident Mach number as initial conditions to predict the triple-point trajectory and the contour of the Mach stems. Bryson and Gross [3] extended Whitham's theory to two- and three-dimensional bodies such as cylinders and spheres by considering analytical formulations. Good agreement has been shown between the experimental and the analytical results. The  $RR \rightarrow MR$  transition in the case of shock-cylinder interaction has been widely investigated in the past. This type of transition is indeed created during the propagation of the shock wave around the cylinder. When the shock wave hits a cylinder, it is first reflected as a regular reflection. The angle between the shock and the tangent to the cylinder surface, at the point of contact on the cylinder, decreases until it reaches the highest point as the shock propagates downstream. This forces the reflection from the cylinder to transit to a Mach reflection. The  $RR \rightarrow MR$  transition criteria have been widely studied in the literature, and the majority of this work, mostly done by Ben-Dor and co-workers (see the most recent work by Rikanati *et al.* [9] and Ben-Dor *et al.* [10], for example), is summarized in his monograph [11]. An experimental study on the propagation of planar shock waves around cylinders of various radii was presented by Heilig [12]. In that work, the theoretical as well as the measured values of the critical angle for the transition from RR to MR were compared for the case of fixed incident shock-wave Mach number. It has been found that the critical angle is independent of the cylinder size but is a function of the strength of the shock wave. In contrast, the dependence on cylinder diameter was studied experimentally by Takayama and Sasaki [13]. They showed that, in addition to the incident Mach number, the  $RR \rightarrow MR$  transition depends on both the radius of curvature of the cylinder (i.e., diameter) and the initial wedge angle, i.e., the angle between the tangent to the cylinder surface (at its leading

---

\*Author to whom all correspondence should be addressed: [sorens@bgu.ac.il](mailto:sorens@bgu.ac.il)

edge) and the direction of propagation of the shock wave. Heilig [12] failed to notice the dependence on the diameter due to the fact that the range of the cylinder diameter was narrow. The load on a cylinder induced by a shock wave was studied by Heilig and Reichenbach [14]. In their work, the unsteady drag force over a circular cylinder placed in a shock tube was determined. The pressure distribution over the cylinder was measured by using pressure gauges distributed over the cylinder. Using holographic interferometry, Takayama and Itoh [15] studied the surface loads generated on a cylinder by a shock wave. They presented experimental results of the pressure distribution around the cylinder along with a drag coefficient distribution.

Since 1970, due to progress in numerical methods, very accurate simulations of shock-wave propagation over obstacles have been developed and used. Most of those studies were focused on the validation of the Euler scheme. For instance, Yang *et al.* [16] investigated the unsteady shock-wave reflection patterns generated by a blast wave propagating over a circular cylinder using an inviscid compressible flow solver with second-order accuracy. The computed pictures of the shock diffraction on a cylinder were compared to the corresponding experimental schlieren pictures taken by Bryson and Gross [3] and were found to be in good agreement. Differences were noticed in region where viscous effects are dominant. Drikakis *et al.* [17] studied numerically the propagation of shock waves over a cylinder using both Euler and Navier-Stokes (NS) codes. The viscous effect, at various Mach numbers, was examined by comparing both inviscid and NS calculations. Computations revealed that the flow-field patterns on the upstream half of the cylinder are not influenced by viscosity, while large differences appear on the downstream half of the cylinder. In a numerical study by Ofengeim and Drikakis [18], the interaction of a planar blast wave with a cylinder was investigated for various blast-wave durations and compared with corresponding results of planar shock waves. As in the previous study, it has been concluded that in the early stage of the shock-wave propagation, the effect of viscosity is negligible. However, during a later stage, particularly when the separation and shock-boundary layer interaction occur, the contribution of the viscosity becomes dominant and the inviscid model can no longer be valid.

The above-mentioned studies did not investigate the behavior of the reflected shock from the cylinder in the upstream direction. The analytical work of Kireev [19] was focused on the axial flow in the vicinity of the stagnation point for the reflection of a strong shock wave from a sphere and a cylinder. To obtain relations that define the time variable of the velocity profile of the reflected wave, a perturbation theory method was used. In that work, the analytical prediction was compared to experimental results and good agreement was found. To the best of our knowledge, no other studies dealing with the dynamics of the reflected-shock wave from a cylinder have appeared in the literature so far.

The present study focuses on the investigation of the reflected curved shock wave from a single cylinder in the weak-shock regime ( $M_s \sim 1-1.4$ ) to characterize the physical parameters affecting its evolution and bring more light and understanding to the complex phenomenon of shock reflection over solid obstacles.

More specifically, in this study new experimental and numerical data for shock propagation are obtained using a shock-tube facility with a new diagnostic system in conjunction with an accurate and robust compressible flow solver. The data are used to investigate the scaling law of the reflected shock at the centerline of the cylinder. Usually, the scaling of the shock propagation and diffraction is based on the compatibility relations, which rely mainly on the global parameters. In the present work, we focus on the local flow properties, including the shock strength and the effect of heat-capacity ratios ( $\gamma$ ), which are the key factors.

This study is the first part of a broader research investigating the interaction of shock waves with complex geometries (such as barriers or corridors) for shock-wave attenuation and practical blast-mitigation design and improvement. The paper is organized as follows: In Sec. II, the experimental setup will be presented followed by a brief description of the numerical approach (Sec. III). Comparisons between Computational Fluid Dynamics (CFD) and experiments are presented in Sec. IV, along with a scaling law of the reflected-shock velocity derived from the obtained data. Finally, conclusions are drawn in Sec. V.

## II. EXPERIMENTAL SETUP

The experimental investigation of the shock-cylinder interaction was carried out in a shock-tube facility at the Shock-Tubes Laboratory of the Protective Technologies R&D Center of Ben-Gurion University. The horizontal shock tube used in this study consists of a 2.3-m-long driver section having a diameter of 80 mm and a 2.5-m-long driven section having a square cross section of 80 mm  $\times$  80 mm. A 1-m-long test section, inside of which the cylinder is placed, is attached to the end of the driven section. The shock wave is formed by rupturing a 0.1–0.25-mm-thick plastic membrane by means of a striking pin. The plastic membrane initially separates the driven section from the driver section. The driver section is pressurized to the required initial pressure. The shock wave interacts with a single cylinder placed in the test section. The 80-mm-long circular PVC-made cylinders spanned across the test section; their diameters are 10, 15, and 20 mm. To allow flow visualization of the test section, two transparent PMMA windows are mounted on the test section sides, permitting a 115 mm  $\times$  56 mm field of view. The cylinder is supported between those two observation windows with the axis of symmetry of the cylinder perpendicular to the direction of propagation of the shock wave. Two pressure transducers are placed 0.5 m apart, one in the driven section and the other in the test section, 80 mm from the cylinder axis. The cylinder is placed at a distance of 258 mm from the end wall. Figures 1 and 2 represent schematic diagrams of the test section and the experimental apparatus, including the shock tube and the diagnostic system, respectively. The timing and control of the system are performed using a National Instruments PCI programmable card (NI-6602) and an in-house developed code using the LabView<sup>®</sup> program.

The main diagnostic system is based on schlieren flow visualization by high-speed photography. The light source for the schlieren system is a double-frequency Nd<sup>3+</sup>:YAG pulsed laser (532 nm) at a rate of 20 000 pulses s<sup>-1</sup>.

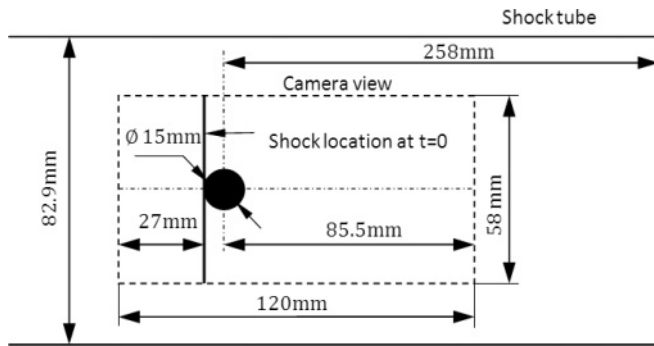


FIG. 1. Experimental configuration. The cylinder is placed in the center of the test section.

The laser produced 240-ns-long pulses with a frequency of 5–50 kHz and an energy of 2.4 mJ pulse<sup>-1</sup>. To monitor the shock-cylinder interaction and the shock-induced flow, a high-speed PHANTOM v12.1 digital camera, capable of capturing images at the appropriate rate of 20 000 frames/s and a resolution of 512×512 pixels, is used. In all the reported experiments, the laser was synchronized with the camera at an approximate rate of 20 000 frames s<sup>-1</sup>, i.e., the time interval between consecutive images is about 50 μs. The exact pulse rate in each experiment is measured by a photodiode and digital oscilloscope. Upon rupturing the plastic membrane, a planar shock wave propagating downstream along the driven section is formed. The passage of the shock over the first pressure transducer, in the driven section, generates a trigger that initiates the camera and the data acquisition system as well, which captures the pressure history. Each laser pulse produces a schlieren image, which is captured and stored in the memory of the high-speed camera. In each experimental configuration, at least three experiments are performed for repeatability. Since there is no synchronization between the laser pulses and the arrival of the shock, the timing of each set of images is different (however, the time difference between images is the same).

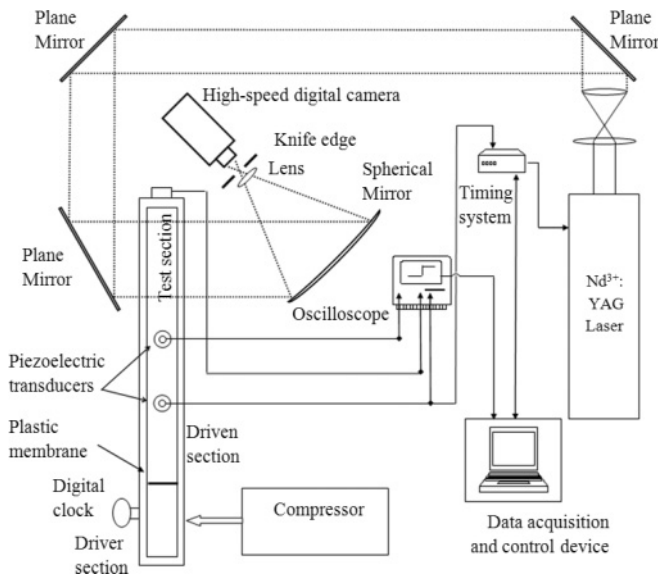


FIG. 2. Schematic diagram of the experimental apparatus including the shock tube, the schlieren system, and the laser light source.

Measurements of the location of the incident shock as well as the reflected shocks in the photographs are obtained using an in-house computerized image-analysis platform based on MATLAB software. The incident shock-wave velocity in the laboratory frame of reference is obtained from a linear fit to the shock-wave locations. Timing of the experimental images is done by finding the first-image time using the location and the velocity of the shock wave. Based on the time of the first image and the known time interval between photographs in all the experiments, the times of the rest of the photographs are determined. The experimental error is influenced by the following measurement uncertainties: the location of the incident shock and the reflected shock waves, the incident shock-wave velocity, the initial time of the experiments, and the calibration error. The total errors of the shock-wave Mach number in all reported data are found to be less than 2%.

### III. NUMERICAL APPROACHES

From the computational viewpoint, a high-order shock-capturing scheme based on a weighted essentially nonoscillatory (WENO) approach is used. This modern class of schemes is very attractive for simulating shock waves, contact discontinuities, and fine-scale flow structures. The WENO schemes use an adaptive “smoothest” substencil chosen within a larger, fixed stencil to construct a high-order approximation of the solution, avoiding the interpolation across discontinuities and preserving a uniformly high order of accuracy at all points where the solution is smooth. The main concept is to use a superposition of several substencils with adaptive coefficients to increase the order of approximations even further. In this paper, we adopt the finite-difference, flux-based, fifth-order WENO scheme with Roe splitting for calculating the numerical fluxes at cell interfaces [20,21]. A robust and stable immersed boundary (IB) method is also developed to deal with complex geometries on Cartesian grids [22]. The developed IB method uses the direct-forcing concept with an efficient interpolation algorithm and accurate boundary forcing expressions.

As a first step toward a partial validation with experiment, viscous effects are neglected. Nonetheless, predictions of instabilities and shock locations are expected to be accurate. These computations are performed bearing in mind a future use of the WENO scheme for shock-turbulence interaction over obstacles. The goal is to assess the resolution properties of the WENO schemes and to gain more physical insight for the problem considered in this study.

A computational domain of size 384 mm × 82.9 mm has been chosen for the numerical simulations. The choice of the domain size is made to avoid any inflow or outflow wave reflections or boundary-layer interaction from the wall of the shock tube. To validate the numerical methods, several test cases, based on steady and unsteady shock-wave propagation, have been previously carried out, along with an extensive grid convergence study. Details of this analysis can be found in Chaudhuri *et al.* [22]. Based on this study, a mesh of 6401 × 1401 grid points is used with a uniformly distributed grid spacing of 60 μm to ensure a grid-independent solution.

In this study, a compressible inviscid model is used to solve Euler equations. The fluid is assumed as a thermally

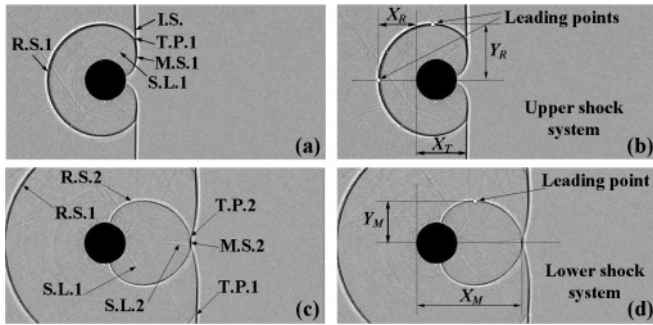


FIG. 3. Main flow features and flow measurements: (a) and (b) Upper shock-wave system; (c) and (d) lower shock system. Notation: I.S., Incident Shock; R.S., Reflected Shock; M.S., Mach Stem; T.P., Triple Point; S.L., Slip Line.

and calorically perfect gas governed by the ideal-gas equation of state.

IV. RESULTS

A. Analysis of the shock-cylinder interaction

Shock-cylinder interaction is studied in the incident-shock Mach number range of  $M_s = 1.1-1.4$  with air as a working gas. In Fig. 3, two typical images obtained from the high-speed photography are presented. In fact, Figs. 3(a) and 3(b) are identical but with different comments in each. This is also true for Figs. 3(c) and 3(d). In Figs. 3(b) and 3(d),  $X_R$  is the horizontal distance from the front of the cylinder to the primary reflected shock (R.S.1),  $X_T$  is the distance from the front of the cylinder to the incident shock (I.S.),  $Y_R$  is the vertical distance from the midline of the cylinder to the highest point of the primary reflected shock (R.S.1),  $X_M$  is the horizontal distance from the front of the cylinder to the secondary Mach stem (M.S.2), and  $Y_M$  is the vertical distance from the midline of the cylinder to the highest point of the secondary reflected shock (R.S.2). The incident shock [I.S. in Fig. 3(a)] propagates along the shock tube from left to right. Owing to the symmetry of the system, a horizontal symmetry plane can be considered through the center of the cylinder.

After the first head-on collision of the shock wave with the cylinder, part of the shock wave is reflected and the remaining part is reflected as a regular reflection over the cylinder surface (figure not shown here for brevity). As the shock wave propagates along the cylinder surface, the point of intersection of the reflected shock (R.S.1) and the incident shock (I.S.) also travels along the cylinder surface. The reflecting wedge angle decreases as the shock propagates and the RR is transformed into MR [see Fig. 3(a)]. The wave pattern, usually designated as the “upper-shock system,” consists of an incident shock (I.S.), a reflected shock (R.S.1), a Mach stem (M.S.1), and a slip line (S.L.1) [see Figs. 3(a) and 3(b)]. The upper-shock system propagates further downstream and grows toward the upper and lower shock-tube sidewalls, while the Mach stems become more curved [Fig. 3(a)]. The two Mach stems created (above and below the symmetry plane) collide behind the cylinder [Fig. 3(c)]. The interaction of the two Mach stems can be considered as a reflection from a solid wall placed at the symmetry plane. From the results, one can see that this reflection is initially regular and then transitions to a Mach

reflection. The new shock pattern propagating downstream of the cylinder is usually designated as a “lower-shock system” and consists of a Mach stem (M.S.1) generated in the “upper shock system,” the reflected shock wave (R.S.2), a Mach stem (M.S.2), and a second slip line (S.L.2) [see Figs. 3(c) and 3(d)]. The reflected-shock wave (R.S.2) travels toward the upper (lower) shock-tube sidewall and is attached to the secondary Mach stem (M.S.2). The point of intersection of the reflected shock (R.S.2), the shock wave (M.S.1), and the Mach stem (M.S.2) belongs to the lower-shock system and is named the second triple point (T.P.2). The other end of the reflected shock wave (R.S.2) travels along the cylinder surface.

B. Qualitative and quantitative comparison between the numerical and experimental results

A set of schlieren images of the shock interaction with a circular cylinder is presented in Fig. 4. The experimental images are presented in the left column of the figure, while the equivalent numerical pictures are shown in the right column. The images are related to the case of a cylinder having  $D = 15$  mm and  $M_s = 1.16$  (see Fig. 1). The frame times indicated for each window are measured with respect to  $t_0$ , where  $t_0$  is

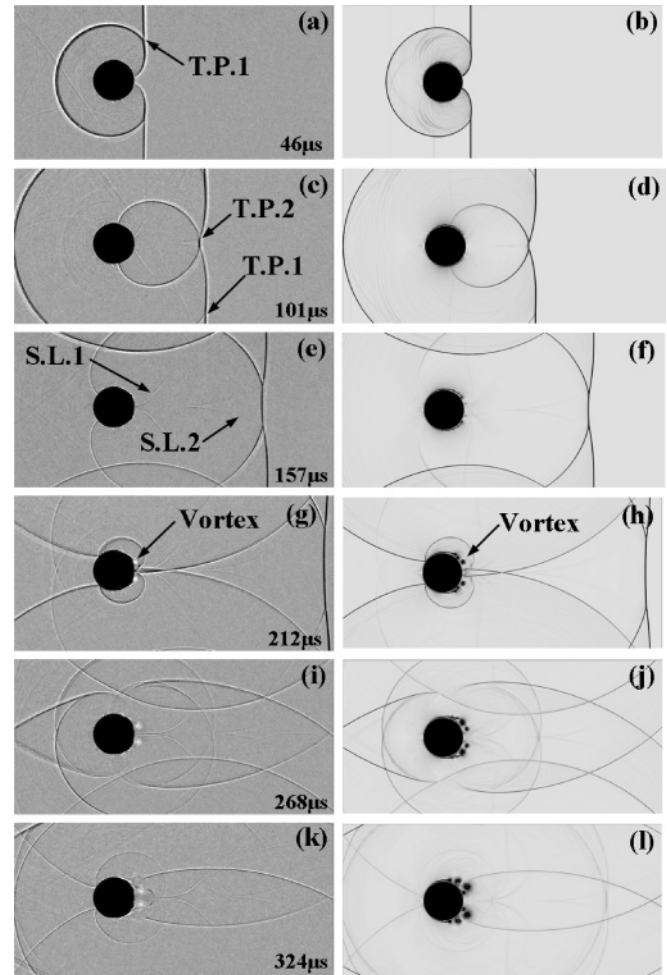


FIG. 4. Comparison of a series of schlieren pictures with the numerical simulation of shock-wave propagation over a 15-mm-diam cylinder,  $M_s = 1.16$ .

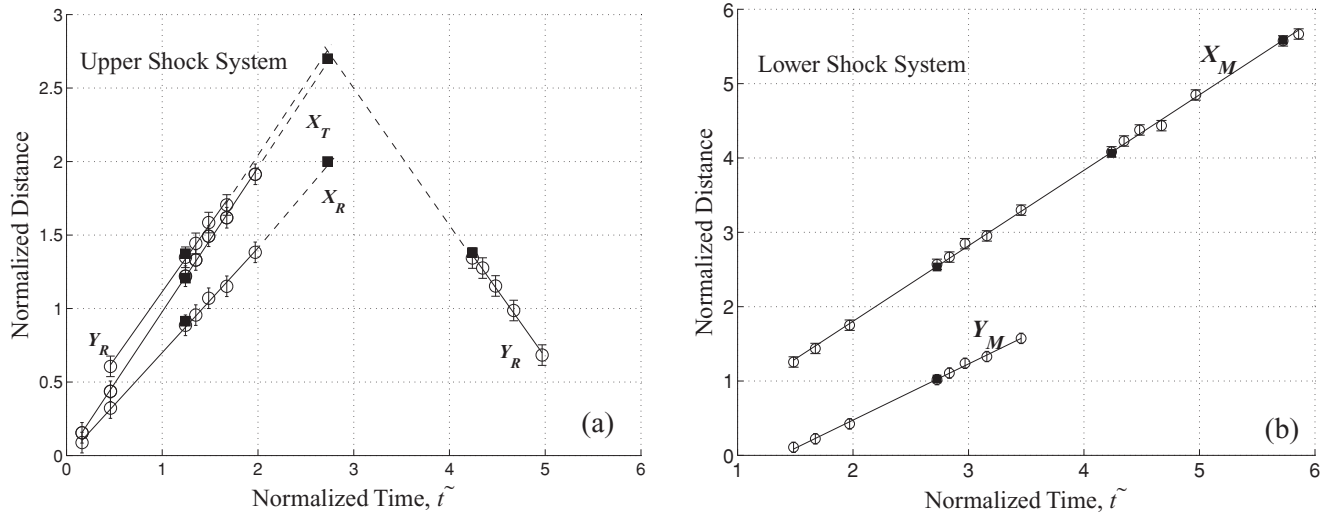


FIG. 5. Location of the reflected shocks in (a) upper and (b) lower shock systems. The  $x$  axis is normalized by  $U_s/D$ .

the time when the incident shock hits the leading edge of the cylinder. The laser nonuniformity and other spots on the images are removed by subtracting the background image from each original image. This leads to a very clean and uniform background, which helps to enhance the observed features.

The I.S. propagates from left to right, impinges on the cylinder surface, and then gets reflected back. As shown in the frame  $t = 46 \mu\text{s}$  [Figs. 4(a) and 4(b)], two upper-shock systems are formed on either side of the symmetry plane.

Two curved Mach stems (M.S.1 and M.S.2) and the corresponding slip surfaces are shown just before the two Mach stems collide. At  $t = 101 \mu\text{s}$  [Figs. 4(c) and 4(d)], the reflected shock from the cylinder (R.S.1) expands upstream toward the shock-tube sidewalls. The two upper shock systems pass the cylinder and collide. Two lower shock systems are formed on either side of the symmetry plane. Two loci of triple points appear symmetrically on the cylinder; the first is initiated on the front side of the cylinder while the second starts on the symmetry plane on the back side of the cylinder. Half of the symmetrical triple-point trajectories are shown in Fig. 5, in which the location of the triple point is measured from the images obtained from the experiments and the numerical simulation. At  $t = 157 \mu\text{s}$  [Figs. 4(e) and 4(f)], the shock (R.S.1) is reflected from the sidewall of the test section and reappears in the camera view while traveling back toward the cylinder.

The reflected shock (R.S.2) generated in the lower-shock-wave system moves on the cylinder surface toward the front stagnation point at one end, and its leading point [Fig. 3(d)] travels toward the shock-tube walls. The Mach stem (M.S.2) on either side of the symmetry plane moves away from the downstream side of the cylinder. Note that one end of the slip surface [denoted S.L.1 in Fig. 3(a)] travels along the cylinder surface and approaches the rear stagnation point. Note that experimental and numerical results are quite comparable for most flow features where the effect of viscosity is negligible, such as triple-point trajectories and diffraction patterns of shock waves. From  $t = 212 \mu\text{s}$  [Figs. 4(g)–4(l)], the reflected shock from the shock-tube walls (cross-stream direction) starts to interact with the cylinder. It can be seen that more complex wave structures start to appear, while the

experimental and numerical features continue to agree in terms of wave locations. However, due to the absence of the diffusion terms in the simulation, discrepancies arise in the loci of the vortex positions on the downstream side of the cylinder. The parameters that are used for quantitative comparisons concern the location of the reflected shocks at different times. The data are recorded from the set of schlieren images and are presented in the  $x$ - $t$  plane with dimensionless coordinates. The flow features presented in Figs. 3(b) and 3(d) are measured in each of the experiments. The locations of the reflected shocks in the upper and lower shock systems obtained from the experiment and the simulation are shown in Fig. 5. The vertical axis (position) is normalized according to the wave position at different times and the cylinder diameter, while the horizontal axis (time) is normalized as  $\tilde{t} = tU_s/D$ , where  $t$ ,  $U_s$ , and  $D$  are the time, incident shock velocity, and cylinder diameter, respectively.

Experimental and computational results for a shock Mach number of  $M_s = 1.16$  are presented in Fig. 5 as follows: open circles are locations of the reflected shocks measured from the experimental images, and black squares are obtained from the simulation. The velocities of the reflected shocks at the measured points are obtained from a linear fit to the locations of the wave with respect to the time interval between the photographs and are constant. In Fig. 5(a), the dashed line represents the trajectory of the reflected wave toward the shock tube sidewalls within the camera view. Note that the locations of the waves measured in the simulations are within the experimental error bars. Excellent agreement is found between the experiment and the numerical simulation for different flow features such as the incident as well as the reflected shock trajectories. This comparison strengthens our confidence in the experimental and simulation results for further investigations.

### C. Investigation of the reflected-shock wave from the cylinder

In this section, a parametric study of the reflected curved shock-wave trajectories is presented. Several numerical computations are realized to investigate the key parameters

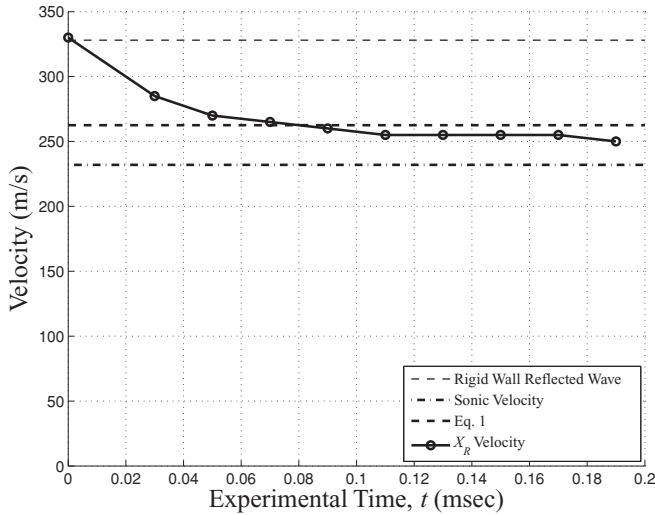


FIG. 6. Velocity of the reflected shock as predicted by the numerical simulation. Solid line, simulation results; thin dashed line, rigid plane wall reflected shock-wave velocity; thick dashed-dotted line, sonic velocity; thick dashed line, prediction of Eq. (1).  $M_s = 1.28$ ,  $D = 15$  mm.

affecting the velocity of the reflected-shock wave. In Fig. 6, the velocity of the leading point ( $X_R$ ) of the reflected shock versus time derived from the numerical data is presented for the case of  $D = 15$  mm and  $M_s = 1.28$ .

It can be seen that, during the first 0.04 ms, the speed of the reflected shock reduces dramatically compared to the speed of a reflected shock from a planar rigid wall [23]. Moreover, it is clear that asymptotically the reflected-shock velocity will reach the sonic velocity, which can be easily explained by the fact that the reflected-shock strength is reduced due to its divergence. These two velocity limits are presented in the figure. The velocity of the reflected shock found in the present work (solid-circle line in the figure) falls between these the two limits. With regard to the scaling law, the objective is

to construct a simple expression based on the obtained data to normalize the velocity of the reflected-shock wave in the vicinity of the cylinder (but not in close proximity to it, i.e.,  $0.05 < t < 0.2$  ms in Fig. 6). The expression should describe the velocity of the leading point ( $X_R$ ) of the reflected-shock wave over the range of  $X_R/D$  from 0.5 to 5.

To evaluate the parameters affecting the reflected-shock velocity, a series of experiments are performed in which shock waves with different intensities collide with cylinders of different diameters (10, 15, and 20 mm) in two different gases (air and  $SF_6$ ). The time evolution of the leading point of the reflected wave ( $X_R$ ) is recorded from numerical and experimental sequences based on schlieren images. The parameters are measured up to the time when the shock wave, getting reflected from the sidewalls, enters the camera’s field of view (see Fig. 1).

Figures 7(a) and 7(b) represent the time evolution of  $X_R$ . The excellent agreement found earlier between the simulation and the experiment permits us to include further numerical results with initial conditions, which are not covered by the experiments. The computed lines are within the error bars. However, in all cases the computational results are slightly higher than the experimental data. These differences are distinguishable in Fig. 7(a). The variation in  $M_s$  produces a notable discrepancy in the reflected-shock velocity. Moreover, as expected, the absolute velocity of the reflected shock decreases due to the increased velocity of the induced flow behind the incident shock. To investigate the effect of the cylinder diameter on the reflected-shock velocity, a set of experiments is performed placing cylinders with different diameters in the test section while keeping  $M_s = 1.16$ . The evolution of  $X_R$  is presented in Fig. 7(a). One can conclude that the effect of the cylinder diameter is small and that the differences fall within the uncertainty bars over the range of the experimental parameters.

To find the relevant parameters affecting the behavior of the reflected-shock wave, nondimensional coordinates are used. The reflected-shock trajectory is plotted using dimensionless

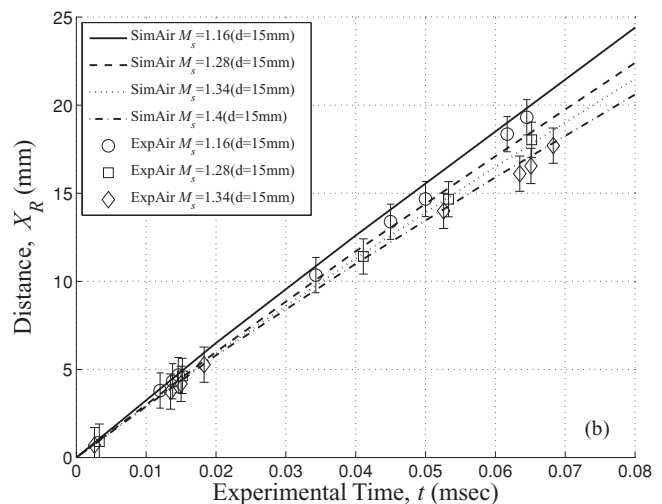
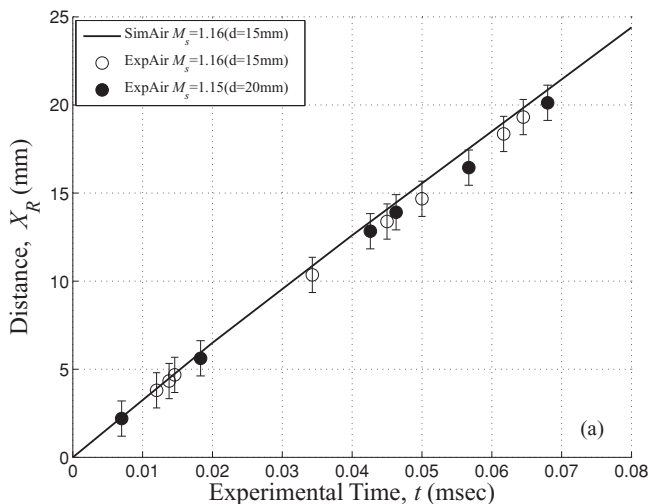


FIG. 7. Location of the leading point,  $X_R$ , of the reflected shock-wave location vs time in air for different initial conditions: (a) Constant incident Mach number ( $M_s = 1.15$ – $1.16$ ) and different cylinder diameters. (b) Constant cylinder diameter (15 mm) and different incident Mach numbers.

coordinates. By finding the appropriate dimensionless time, the data from various experiments with different initial conditions collapse into a single curve. From the data analysis, the following linear relationship between the velocity ratio (the reflected-shock velocity from the cylinder divided by the reflected-shock velocity from a planar end wall) and the Mach number is found:

$$1 - \frac{U_R}{U_{RW}} = f(\gamma)(M_s - 1) \quad (1)$$

The scaling function  $f(\gamma)$  includes other parameters that have not yet been tested up to this point. The value of this function is found to be constant and equal to 0.714 for  $\gamma = 1.4$ . This value is obtained from a linear fit of the obtained results presented in Fig. 7(a) to Eq. (1). As can be seen from Figs. 7(a) and 7(b), the  $U_R$  for each experiment can be approximated to a constant (a linear fitting). Thus, it can be written as

$$U_R t = U_{RW} [f(\gamma)(M_s - 1)] t \quad (2)$$

and in dimensionless coordinates, with  $X_R = U_R t$ ,

$$\frac{X_R}{D} = \frac{U_{RW} t}{D} [1 - f(\gamma)(M_s - 1)]. \quad (3)$$

As an initial estimation, the right-hand side of Eq. (3) can be identified as a dimensionless time, so that

$$\tilde{t} = \frac{U_{RW} t}{D} [1 - f(\gamma)(M_s - 1)]. \quad (4)$$

The location of the reflected-shock-wave leading points, obtained from series of the experiments and numerical simulations for  $f(1.4) = 0.714$  as found earlier, is normalized by the cylinder diameter,  $D$ , and plotted as a function of the new scaled time (see Fig. 8).

By applying this normalization [Eq. (4)], all experimental and computational results collapse together into a single straight line. Moreover, further simulations with longer time confirm the same trends. It should be noted that the procedure performed here is based on the approximation of a constant reflected shock velocity (see Fig. 6).

To clarify the expression of  $f(\gamma)$ , further studies are performed with different gases, keeping the same test configuration. Experiments and simulations are conducted using SF<sub>6</sub> (with  $\gamma = 1.09$ ).

Figure 9 presents two typical images of the shock-wave diffraction for SF<sub>6</sub> with  $D = 15$  mm. The time interval between the two sequences is 56  $\mu$ s. The shock-wave diffraction patterns evolve similarly to the case of air. A distinguishable difference can be observed in the strong vortices formation downstream of the cylinder. As can be seen in Fig. 9(a), a  $\lambda$ -shock-wave configuration is formed at the rear side of the cylinder, and 56  $\mu$ s later the vortex is beginning to detach and travel downstream [Fig. 9(b)]. Analyzing these effects is beyond the scope of the present paper; however, the locations of  $X_R$  are extracted from both experimental and computational data.

Figure 10 presents the combined results of the  $X_R$  measured from the experiments and numerical simulations in different gases (air and SF<sub>6</sub>) for a cylinder diameter of 15 mm and different incident Mach numbers. The points are obtained from the experiments and the curves from the simulations. As can

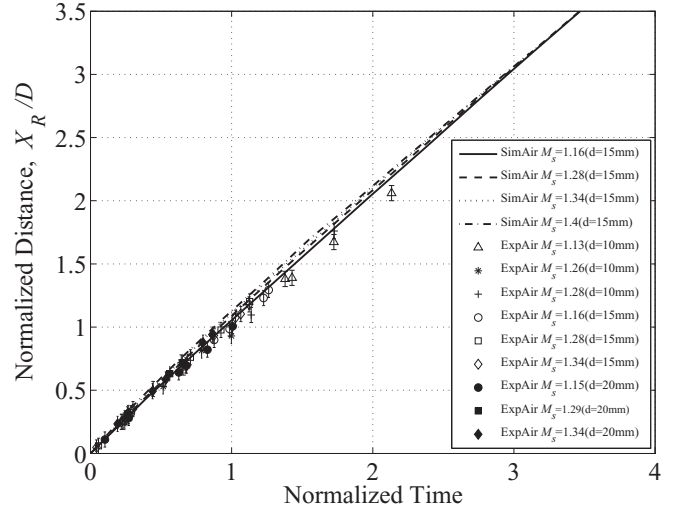


FIG. 8. Normalized reflected shock-wave location vs normalized time for different flow configurations. The time is normalized as in Eq. (4).

be seen, the reflected-shock velocities for both air and SF<sub>6</sub> decrease with increasing incident shock-wave Mach number. The reflected-shock velocities in SF<sub>6</sub> are smaller than those in air.

After a trial and error process, it is found that all curves collapse if  $f(\gamma) = 1/\gamma$ . Inserting this expression into Eq. (4) results in the following new time scaling:

$$\tilde{t} = \frac{U_{RW} t}{D} [1 - (M_s - 1)/\gamma]. \quad (5)$$

To broaden the spectrum of the investigated parameters, a new set of simulations is performed using argon ( $\gamma = 1.667$ ) as a working gas for different values of  $M_s$ . Figure 11 represents the normalized shock location along the line of symmetry as a function of  $\tilde{t}$  [see Eq. (5)] for different test gases (air, Ar, and SF<sub>6</sub>) and different  $M_s$  and  $D$ . As can be seen, all data fall closely onto a single curve, which shows that the approximate relation presented in Eq. (5) is a suitable time scaling for the reflected-shock trajectory,  $X_R$ , from a rigid cylinder for different incident-shock Mach numbers, different cylinder diameters, and different gases. However, there are still minor discrepancies between different data, probably due to the empirical character of the formulation. A detailed analytical solution, if possible, should reveal the exact expression.

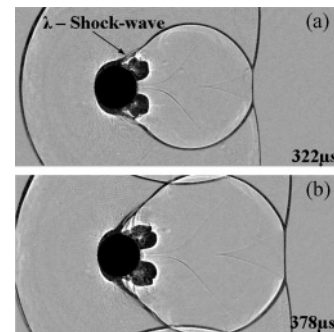


FIG. 9. Schlieren image of the shock-wave interaction with a 15-mm-diam cylinder in SF<sub>6</sub>,  $M_s = 1.28$ .

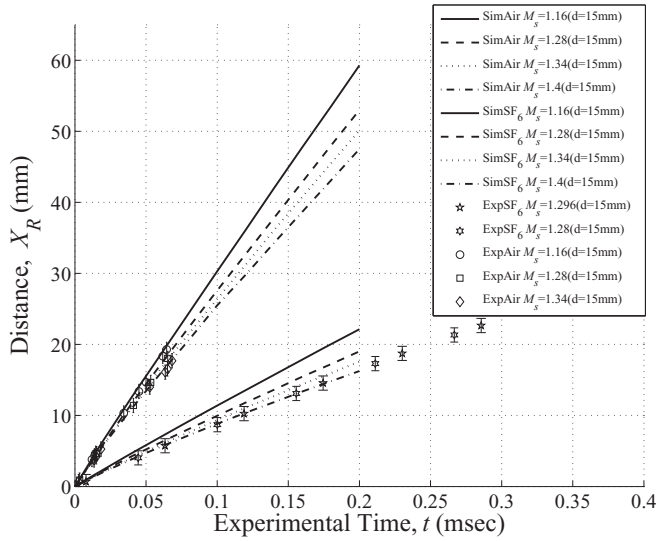


FIG. 10. Reflected wave location vs time from the experiments and simulations done with different gases in the case of a 15-mm-diam cylinder.

To express the obtained results using only the initial conditions, one can use the expression of the reflected-shock velocity as presented in [23], Eq. 4.1.57, and the well-known relation (see Ref. [23], Eq. 4.1.34)

$$U_{RW} = \frac{2\xi + \alpha - 1}{\sqrt{(1 + \alpha)(1 + \alpha\xi)}} a_0, \quad (6)$$

where  $\xi$  is the shock strength defined as

$$\xi = 1 + \frac{2\gamma}{(\gamma + 1)} \beta, \quad (7)$$

where  $\beta = M_s^2 - 1$ ,  $\alpha = (\gamma + 1)/(\gamma - 1)$ , and  $a_0$  is the sound velocity in the unshocked fluid. After some algebraic

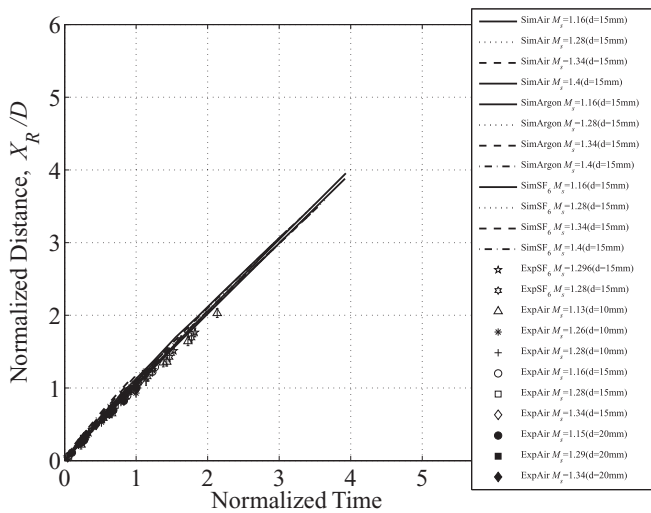


FIG. 11. Reflected wave location vs time from experiments and simulations for different gases. The time is normalized as in Eq. (5).

manipulation, one gets

$$U_{RW} = \frac{1}{M_s} (1 + 2\alpha^{-1}\beta) a_0. \quad (8)$$

Implementing relation (8) into Eq. (3) and using  $f(\gamma) = 1/\gamma$ , one can obtain the reflected-shock trajectory:

$$\frac{X_R}{D} = \frac{a_0 t}{D} \frac{1}{M_s} (1 + 2\alpha^{-1}\beta) \left(1 - \frac{M_s - 1}{\gamma}\right). \quad (9)$$

For further validation, numerical simulations are carried out for longer times than the experiments. It appears that, as time evolves, the computed lines approach each other, strengthening our confidence in the proposed scaling law. However, this scaling is tested for larger Mach numbers and found to be not valid for  $M_s > 1.4$ , showing thereby the limit of applicability of the proposed formulation.

As discussed above, the velocity extracted from Eq. (1) lies in between two asymptotic cases: the reflected-shock velocity from a planar rigid wall as the upper limit and the sonic velocity in the shocked gas as the lower limit. These two cases are emphasized in Fig. 6 together with the actual reflected-shock velocity from a cylinder found in the simulations.

According to Eq. (9), it seems that the evolution of the reflected-shock trajectory can be approximated by the velocity of a shock wave reflected from a planar rigid wall reduced by the factor  $1 - (M_s - 1)/\gamma$ .

## V. CONCLUSIONS

In this study, the interaction of planar shock waves with circular cylinders is investigated both experimentally and numerically. The experiments are carried out in a shock tube with a schlieren-based diagnostic system. The numerical method is based on a fifth-order WENO scheme solver for the Euler equations in conjunction with an immersed boundary technique. The study has focused on the behavior of the reflected curved shock wave from the cylinder in the upstream direction.

It has been found that the velocity of the leading point of the reflected wave can be approximated by a simple universal relation. The velocity is proportional to the reflected-shock velocity from a planar rigid wall reduced by a factor that depends on the incident shock-wave Mach number and the heat capacities ratio. The proposed relation is valid in the limit of weak shock waves ( $M_s < 1.4$ ). This relation is obtained under the assumption that the velocity of the leading point of the reflected-shock wave is constant. In our opinion, at Mach numbers higher than 1.4, compressible effects start to play an important role in the dynamics of the flow, and the assumption of constant reflected shock velocity is no longer valid in this case. However, additional investigations are needed for further verification of this assumption. Nevertheless, the derived relation is valid in the range of  $0.5-5 D$  from the cylinder, but certainly not closer than  $0.1 D$ . It is believed that the assumption is valid to longer distances. However, since no measurements are conducted beyond this region, the conclusions of the present study are limited to this region. This study is part of a more comprehensive investigation of the interaction of moving shock waves with obstacles.

## ACKNOWLEDGMENTS

The authors would like to thank G. Ben-Dor, Y. Kivity, A. Britan, and A. L. Levin from Ben-Gurion University of the Negev for fruitful discussions during the course of this study.

This research is supported by The Israel Science Foundation (Grant No. 139/10). Computations were performed using HPC resources from GENCI (CCRT/CINES/IDRIS) (Grant No. 2010-0211640), France.

- 
- [1] G. Ben-Dor, J. M. Dewey, and K. Takayama, *J. Fluid Mech.* **176**, 483 (1987).
  - [2] H. Li, G. Ben-Dor, and Z. Y. Han, *Fluid Dyn. Res.* **14**, 229 (1994).
  - [3] A. E. Bryson, R. W. Gross, and Z. Y. Han, *J. Fluid Mech.* **10**, 1 (1961).
  - [4] P. W. Duck, *J. Fluid Mech.* **214**, 611 (1990).
  - [5] A. Kluwick, P. Gittler, and R. J. Bodoni, *J. Fluid Mech.* **140**, 281 (1984).
  - [6] M. Adravkovich, *Flow Around Circular Cylinders. Vol. 2: Applications* (Oxford University Press Inc., New York, 2003).
  - [7] S. Chang and K. Chang, *Shock Waves J.* **10**, 333 (2000).
  - [8] G. Whitham, *J. Fluid Mech.* **2**, 145 (1957).
  - [9] A. Rikanati, O. Sadot, G. Ben-Dor, D. Shvarts, T. Kuribayashi, and K. Takayama, *Phys. Rev. Lett.* **96**, 174503 (2006).
  - [10] G. Ben-Dor, M. Ivanov, E. I. Vasilev, and T. Elperin, *Prog. Aerospace Sci.* **96**, 347 (2002).
  - [11] G. Ben-Dor, *Shock Wave Reflection Phenomena* (Springer-Verlag, New York, 1992).
  - [12] W. Heilig, *Phys. Fluids Suppl. I* **12**, 154 (1969).
  - [13] K. Takayama and M. Sasaki, *Reports of the Institute of High Speed Mechanics* (Tohoku University, Sendai, Japan, 1983), Vol. 46, p. 1.
  - [14] W. Heilig and H. Reichenbach, *Proceedings of the 6th International Symposium on Military Applications of Blast Simulations, Cahors, France, 1.7.1* (Centre d'Etudes de Gramat, Gramat, France, 1979).
  - [15] K. Takayama and K. Itoh, *Reports of the Institute of High Speed Mechanics* (Tohoku University, Sendai, Japan, 1986), Vol. 51, p. 1.
  - [16] J. Yang, Y. Liu, and H. Lomax, *AIAA J.* **25**, 683 (1987).
  - [17] D. Drikakis, D. Ofengeim, E. Timofeev, and P. Voionovich, *J. Fluids Struct.* **11**, 665 (1997).
  - [18] D. Ofengeim and D. Drikakis, *Shock Waves J.* **7**, 305 (1997).
  - [19] V. T. Kireev, *Fluid Dyn.* **4**, 19 (1969).
  - [20] G. Jiang and C. W. Shu, *J. Comp. Phys.* **126**, 202 (1996).
  - [21] E. M. Taylor, M. Wu, and P. Martin, *J. Comp. Phys.* **223**, 384 (2007).
  - [22] A. Chaudhuri, A. Hadjadj, and A. Chinnayya, *J. Comp. Phys.* **230**, 1731 (2011).
  - [23] G. Ben-Dor, O. Igra, and T. Elperin, *Handbook of Shock Waves* (Academic, San Diego, 2000).